Computation of the flow around a hyperboloid flare (T1-97), a hollow cylinder (T2-97)and an ogive cylinder (T3-97) VKI Contribution to the HSFF2 Data Base Workshop.

W. Dieudonné *
E. van der Weide †
H. Deconinck ‡
J.-M. Charbonnier §
von Karman Institute for Fluid Dynamics
Chaussée de Waterloo, 72 - B-1640 Rhode-St-Genèse, Belgium

In the framework of the First High Speed Flow Field Database Workshop Part II (HSFF-2), a standard finite volume code on structured grids and a newly developed multidimensional residual distribution code on unstructured grids are validated and compared.

Several test cases are treated covering a wide range of geometries (axisymmetric hyperboloid flare and hollow flare / three-dimensional ogive cylinder) and flow regimes (supersonic and hypersonic, laminar and turbulent). First the two codes are briefly presented and described, then the results are compared to each other and to experimental data when available.

Introduction

The HSFF2 workshop proposes to assemble new information to validate numerical methodologies in supersonic and hypersonic flow fields. A structured grids finite volume code and an unstructured grids residual distribution code, both developed at the VKI, are validated for a large set of flow regimes. Axisymmetric and three-dimensional problems are treated for supersonic and hypersonic flow fields, for both laminar and turbulent regimes. The spatial discretisations, the acceleration techniques and the turbulence models used are briefly discussed. Attention is focused on the code results which are compared to each other and to experimental data when available.

Numerical methods

Finite volume code

The VKI-MB structured grids code is based on a finite volume upwind formulation[1] using Van Leer, Roe or hybrid[2] Riemann solvers. The Navier-Stokes equation is solved in its axisymmetric form which writes:

$$\frac{\partial Q}{\partial t} + \frac{\partial F}{\partial x} + \frac{\partial G}{\partial y} + H = \frac{\partial F_v}{\partial x} + \frac{\partial G_v}{\partial y} + H_v \tag{1}$$

where Q is the vector of conservative variables and H, H_v denote the axisymmetric source terms. The inviscid fluxes are F, G, H and the subscript v stands for the viscous contribution.

Turbulence modelling is achieved through the Spalart-Allmaras one equation turbulence model[3] which solves for the turbulent viscosity obtained through the transport equation:

$$\begin{aligned} \frac{D\tilde{\nu}}{Dt} &= c_{b1}\left[1 - f_{t2}\right]\tilde{S}\tilde{\nu} \\ &+ \frac{1}{\sigma}\left[\nabla.((\nu+\tilde{\nu})\nabla\tilde{\nu}) + c_{b2}(\nabla\tilde{\nu})^2\right] \\ &- \left[c_{w1}f_w - \frac{c_{b1}}{\kappa^2}f_{t2}\right]\left[\frac{\tilde{\nu}}{d}\right]^2 \\ &+ f_{t1}\Delta U^2 \end{aligned} \tag{2}$$

Following the implementation of this model,[4] high speed flow problems[5] have been studied for both internal and external aerodynamics.

The computations presented are carried out using an explicit Runge-Kutta integration scheme. For some cases, a full approximation storage multigrid scheme[6,7] is employed to accelerate convergence rates. The strategy of the multigrid technique is to couple different grid levels in order to cover a larger frequency spectrum in which each particular grid is responsible for damping out a specific frequency bandwidth. It is this full approximation storage scheme which has been implemented in the code.[8] A standard V cycle is used and the inter-grid operators are constructed from bi-linear interpolation which is found to be fast and accurate enough.

A new code, which is under development and has not been fully validated yet, also based on a finite volume scheme, will be used to do some of the 3D computations. It is programmed in Fortran 90 using object orientation and it solves the 3D Navier-Stokes equations for laminar flows on structured grids with

*PhD candidate
†PhD candidate
‡Professor, head of numerical simulations
§Assistant Professor, high speed flows

either van Leer or Roe's Riemann solvers. Second order accuracy in space is obtained using the MUSCL interpolation technique; a four step Runge-Kutta explicit scheme is used for second order time accurate solution. Future developments will be carried out in order to include turbulence modeling and acceleration techniques.

Residual distribution code

The multi-dimensional upwind method is well-established nowadays for scalar convection-diffusion problems for which it leads to improved schemes with compact stencils compared to the standard finite volume schemes based on MUSCL reconstruction.[9–11] The generalization to coupled systems has been made recently[12,13] and is constructed such that for any decoupled equation in the system it automatically reduces to the scalar distribution scheme on which it is based. The Petrov-Galerkin finite element interpretation of the schemes[11,13,14] allows a straightforward discretization of the viscous terms. Through integration by parts, the discretization of these terms on linear elements boils down to the Galerkin method.

System Distribution Schemes

The discretization of a general non-commuting hyperbolic system is briefly discussed.[12,13] Consider the unsteady hyperbolic system of equations in two space dimensions, given by

$$\frac{\partial U}{\partial t} + A_U\frac{\partial U}{\partial x} + B_U\frac{\partial U}{\partial y} = 0. \tag{3}$$

and assume further that this system has been linearized over a triangular computational cell T (see next section) such that the Jacobian matrices A_U and B_U are constant. The geometry of the cell is given in figure 1. Using Gauss' theorem the residual in integral form of equation (3) over cell T is

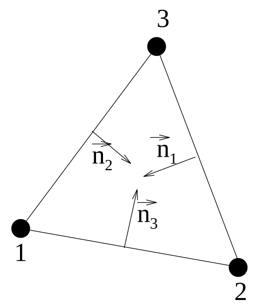

Fig. 1 A generic triangle with its inner scaled normals

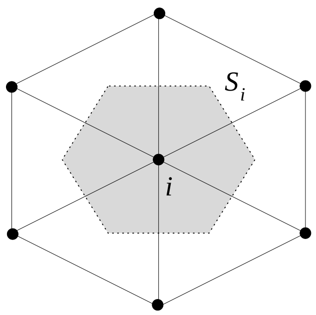

Fig. 2 Area of the median dual cell S_i of node i

$$\begin{aligned}\Phi^T &= \iint_T \left(A_U\frac{\partial U}{\partial x} + B_U\frac{\partial U}{\partial y}\right) d\Omega \\ &= \oint_\Gamma \left(A_U n_{x_{ext}} + B_U n_{y_{ext}}\right) U \, d\Gamma,\end{aligned} \tag{4}$$

where Φ^T is the vector containing the cell residuals, Γ is the boundary of the control volume T and $n_{x_{ext}}$ and $n_{y_{ext}}$ are respectively the x and y component of the outward normal. In the residual distribution approach, the contour integral is evaluated using the unknowns stored at the corners, and fractions of Φ^T are sent to the cell vertices. Assembling the contributions from all cells the nodal update is obtained. The semi-discretization in point i with lumped Galerkin mass matrix is then

$$\frac{dU_i}{dt} = -\frac{1}{S_i}\sum_T \beta_i^T \Phi^T. \tag{5}$$

Here S_i is the area of the median dual cell around node i, see figure 2, and β_i^T is the distribution matrix to node i. For consistency, one has $\sum_j \beta_j^T = I$, where the summation extends over all 3 vertices of the triangle.

The properties of the different schemes are determined by the way β_i^T is defined. Important properties are Positivity (monotonicity) and Linearity Preservation (second order accuracy). It can be proved that only non-linear schemes can satisfy both properties at the same time (Godunov's theorem).

In the computations, a monotone first order scheme (N-scheme) and its second order limited counterpart (PSI-scheme) have been used.

Conservative linearization

For the positivity property, it is essential that the quasi-linear form of the equations in combination with constant Jacobian matrices per cell is used. To capture the discontinuities with the correct jump relations the numerical scheme must be based on the conservative form of equation (3),

$$\frac{\partial U}{\partial t} + \frac{\partial F}{\partial x} + \frac{\partial G}{\partial y} = 0, \tag{6}$$

where F and G are the flux vectors in respectively x and y direction.

The link between the two formulations is the conservative linearization, which requires that the integral form of both equations are equal. If the convective fluxes of the conservative form (6) and the corresponding terms of the quasilinear form (3) are integrated over a control volume, with the assumption of constant Jacobian matrices per cell, and both expressions are required to be equal, the following conservation constraint is obtained:

$$\iint_T \left(\frac{\partial F}{\partial x}+\frac{\partial G}{\partial y}\right) d\Omega \equiv \left(A_Z(\bar{Z})\vec{1}_x + B_Z(\bar{Z})\vec{1}_y\right)\cdot \iint_T \left(\frac{\partial Z}{\partial x}\vec{1}_x+\frac{\partial Z}{\partial y}\vec{1}_y\right) d\Omega. \tag{7}$$

and $\bar{Z}$ is the arithmetic average of the corner values of the triangle.[13] For the Euler equations, the set of variables Z is given by the Roe parameter vector

$$Z=\sqrt{\rho}\,(1\ u\ v\ H)^T \tag{8}$$

with the specific heat ratio γ assumed to be constant.

The extension of the system distribution schemes and the conservative linearisation to three space dimensions, where the control volumes are tetrahedra, is straightforward and will not be discussed.

Time integration

The spatial discretisation leads to a set of ordinary differential equations in time (5), which for convenience sake is written as

$$\frac{dU}{dt}=R\,(U) \tag{9}$$

where $R(U)$ is a complicated nonlinear function of the solution U. This system is integrated in time until the steady state is reached. Explicit methods have the advantage of being extremely simple to implement and are quite robust. However, especially for turbulent flow, the time step limitation is so restrictive that the CPU time requirement becomes unacceptably long, especially in 3D. One way to improve this is multigrid as used in the structured grid code. Another possiblity is the use of implicit methods. As the steady state solution of equation (9) is independent of the time integration method, the backward Euler method is used. After linearization of the right hand side $R(U)$ the following linear system is obtained

$$\left(\frac{I}{\Delta t}-\left(\frac{\partial U}{\partial R}\right)^n\right)\left(U^{n+1}-U^n\right)=R\,(U^n)\,. \tag{10}$$

The Aztec library[15] of Sandia National Laboratories is used to solve this sytem with preconditioned Krylov iterative methods on parallel platforms. This library has been programmed in such a way that the parallelisation process is almost hidden for the user.

The time step in (10) is chosen as

$$\Delta t = CFL\,(\Delta t)^{st}\,, \tag{11}$$

where $(\Delta t)^{st}$ is the time step obtained from a local stability analysis of the forward Euler time integrator[13] and CFL is a number chosen by the user, which varies during the iterative procedure.

Turbulence modelling

The effect of turbulence is modelled by a turbulent viscosity approximation. This eddy viscosity is computed using Menter's two equation shear-stress transport (SST) model,[16] which is a blending between the $k-\epsilon$ and $k-\omega$ models. Furthermore an additional modification is added to account for the transport of the turbulent shear stress. This modification allows better prediction of flows with adverse pressure gradients.

The additional equations are scalar advection-diffusion equations with source terms. The discretisation of the advection-diffusion part is straight forward and only the source terms require special attention. These are split into a positive and a negative part, *i.e.* $S=S^+ + S^-$, where S^+ is the production term and S^- the destruction term. For stability reasons only the destruction term is linearised in equation (10), which increases the diagonal dominance of the linear system. To improve the stability even more, the turbulent equations are solved decoupled from the main flow equations. An additional advantage of this approach is a saving in memory of a factor two.

Results

The full description of the test cases geometries is given in the workshop data base. For each test case, the flow conditions are recalled and the interesting flow properties are briefly shown.

T1-97 Hyperboloid flare

Laminar flow: case T1-97.1

For the finite volume code, the grid is generated by a 2 dimensional hyperbolic grid generator and has 401x101 points. The height of the first cell at the flare junction is $6.9*10^{-6}$ m. Because of the flare, a recirculation bubble appears and produces a relatively complex flow field with lambda type compression shocks associated to the separation and reattachment of the boundary layer. Figure 3 shows the iso Mach lines over the model.

The first flow conditions (T1-97.1) are:

M_∞	6.78
Re_∞	$7*10^6/m$
T^0_∞	600 K
T_{wall}	296 K
L	0.05924 m

An explicit scheme is employed with a 4 steps Runge-Kutta integration. Grid sequencing is used with two grid levels (100x50, 200x100) to obtain a good flow initialisation on the fine grid. This also allows to look at the grid convergence which is known to be difficult to achieve when flow separation is present. As the convergence on the fine grid level is too slow, a multigrid scheme is used with the two previously mentioned grid levels. As seen in figure

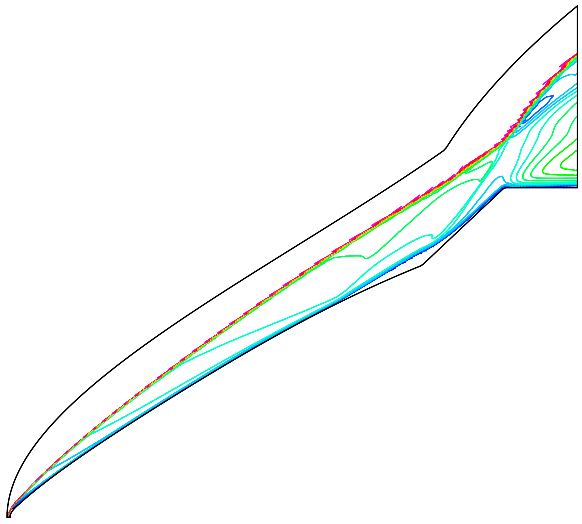

Fig. 3 Mach number isolines for T1-97.2

4 for the convergence history, a strong improvement can be achieved.

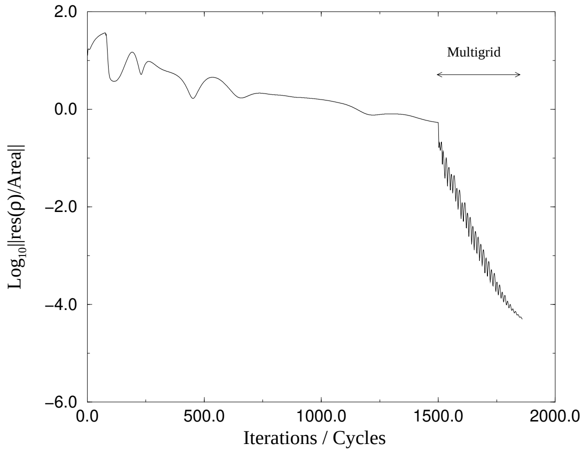

Fig. 4 Convergence history for T1-97.2 - finite volume code

The residual distribution code is also used on the same grid for which each quadrilateral is divided into 2 triangles. This allows to compare the results obtained from the two codes using a different spatial discretisation.

The flow initialisation on the fine grid is obtained through interpolation of the results on a coarse grid. This first order coarse grid solution has been computed with a starting CFL number of 1.0 and multiplied every time step by 1.1, until a maximum of 5.0. The CFL number has been kept constant at this value until the solution has converged one order of magnitude, after which it is increased again by a factor 1.5 per time step until a maximum of 10^6. On the fine grid the starting CFL number for the first order computation is 1.0 and increased every time step until a maximum of 10^6. For the second order computation, with first order Jacobians, the same CFL strategy has been followed, only the maximum CFL has been limited to 100. The convergence history is shown in figure 5. For the first order Navier-Stokes computation, zero machine accuracy is reached. For the second order computation the solution converges two orders of magnitude and then stalls. This is typical for the limited second order PSI scheme presently used. Experience has shown that the solution at this level is converged within truncation error if a sufficiently high CFL can be taken (O(100)).

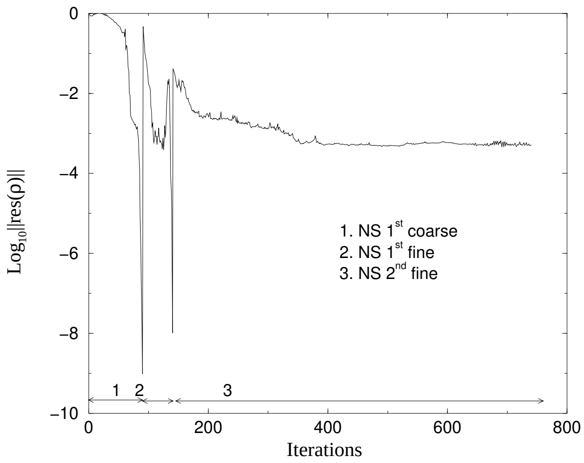

Fig. 5 Convergence history for T1-97.2 - residual distribution code

Figures 6, 7 and 8 for the pressure coefficient, the Stanton number and the skin friction coefficient, compare the results of the two codes.

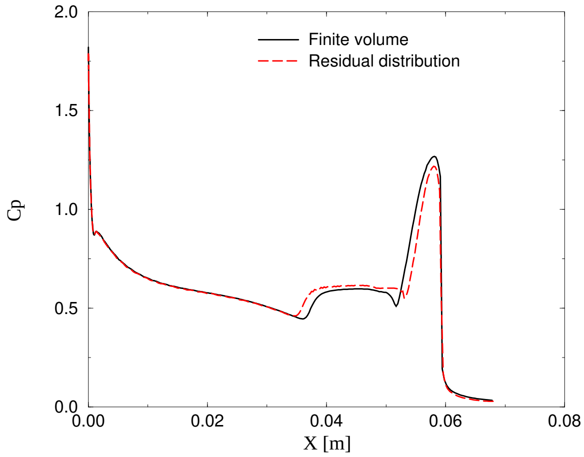

Fig. 6 Pressure coefficient on the hyperboloid flare - Codes comparison for T1.97.1

As expected, the wall data are very similar on the hyperboloid part where the boundary layer is attached. However, the residual distribution scheme detects the boundary layer layer separation point upstream of the finite volume code.

Turbulent flow: case T1-97.2

This computation has been carried out with the structured code only.

The flow conditions for the turbulent boundary layer on the hyperboloid flare (case T1-97.2) are:

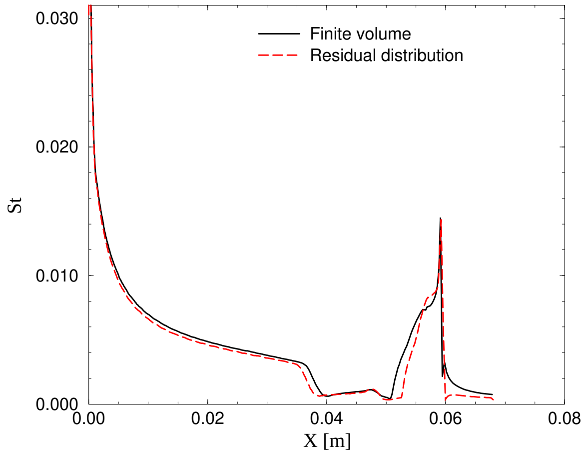

Fig. 7 Heat flux coefficient on the hyperboloid flare - Codes comparison for T1.97.1

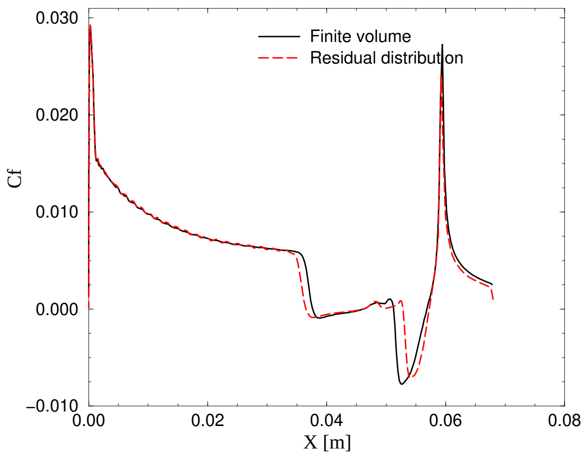

Fig. 8 Skin friction coefficient on the hyperboloid flare - Codes comparison for T1.97.1

M_∞	6.85
Re_∞	$14.8 * 10^6/m$
T^0_∞	600 K
T_{wall}	310 K
L	0.05924 m

From the experimental data (e.g. heat flux) the boundary layer seems to be laminar up to the separation point and turbulent on the flare section of the hyperboloid flare. Thus the boundary layer transition is located in a region within the bubble.

To investigate the flow over the hyperboloid flare, it was decided first to carry out a fully laminar computation and then to place the transition from laminar to turbulent either at the separation point or at the reattachment point.

The laminar computation indicates the separation and reattachment location. The location of the laminar separation point corresponds to the transition location for the first turbulent computation. Also, the location of the laminar reattachment point will be used as the location of the transition location for the second turbulent computation.

With the finite volume code, the separation of the boundary layer on the fine grid occurs at x=38.93 mm, the reattachment is at x=55.90 mm.

For the turbulent computation with the one equation turbulence model of Spalart-Allmaras, the source term does not appear to be large enough with respect to the destruction term and the turbulent profile is not created. Thus one of the functions of the model is artificially increased:

$$\begin{aligned} &g_t \equiv min\left(0.1, \Delta x_t \frac{\Delta U}{\omega_t}\right) \\ &to \\ &g_{t-modif} = 0.1 \end{aligned} \qquad (12)$$

However, this leads to instabilities[5] in the propagation of the turbulent quantity.

Thus the one equation model is coupled with an algebraic model (Baldwin-Lomax) which is used as a starter to define an initial profile for the turbulent quantity. This technique also brings a large gain in computational time because the process of establishing the turbulent profile with the Spalart-Allmaras model is slow.

The results for the three cases: fully laminar (type I), turbulent from the separation (type II) and turbulent from the reattachment (type III) are summarised in the next table which gives the location of the recirculation bubble:

Grid	Type	x_s [mm]	x_r [mm]	Δx_s
101x26	I	44	55	0.10
101x26	II	49	51	0.01
101x26	III	42	54	0.12
201x51	I	40	46	0.16
201x51	II	48	51	0.03
201x51	III	40	55	0.15
401x101	I	39	56	0.18
401x101	II	46	51	0.06
401x101	III	39	55	0.18

Table 1 Location of separation and reattachment points - T1-97.2

where Δx_s is defined as:

$$\Delta x_s = \frac{x_{hinge} - x_s}{x_{flare}} \qquad (13)$$

with $x_{hinge} = 4.9367 * 10^{-02}$m and $x_{flare} = 5.9240 * 10^{-02}$m.

Tests in the RWG wind tunnel have been carried out on the hyperboloid-flare geometry[17,18] and pressure and heat flux data are available.

For the pressure coefficient, figure 9 shows that the turbulent case, for which the transition is located at the separation point obtained from the laminar computation, does not produce correct results. The size of the recirculation bubble strongly underpredicts the experimental data. It can be noted that the

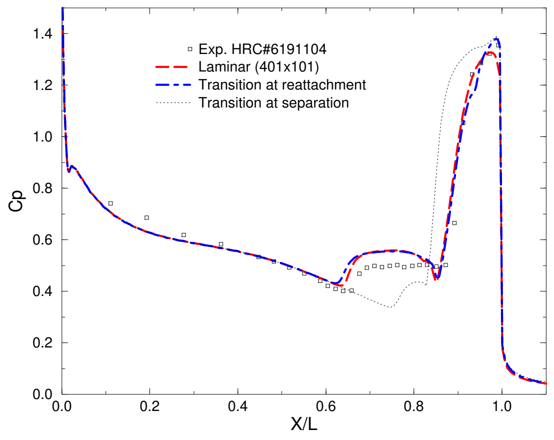

Fig. 9 Wall pressure for T1-97.2

peak pressure predicted for the three cases is hardly affected.

The case producing the best agreement with the experimental data is for the transition placed at the reattachment. Table 2 compares the experimental and numerically obtained values for the recirculation bubble.

Experiment[17,18]	L_{sep}/L	Numerics	L_{sep}/L
pressure	0.185	C_p	0.203
oil flow	0.183	C_f	0.186
liquid crystals	0.156	St	0.200

Table 2 Experimental and predicted location of the separation point T1-97.2

For the heat fluxes, the comparison between the experimental data and the numerical data shows the strong influence of the change in the boundary layer properties as seen in figure 10.

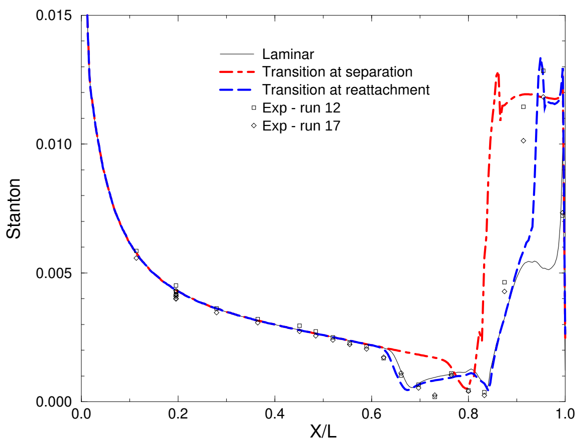

Fig. 10 Wall heat flux for T1-97.2

The laminar case strongly underpredicts the peak heat flux on the flare section indicating that the boundary layer in this region is turbulent. The case for which the transition is placed at the separation shows that the recirculation bubble is missed, tripping the boundary layer brings energy which delays the separation onset. Therefore the boundary layer transition can not be upstream of the separation point obtained assuming a laminar boundary layer. For the last case, which assumes a turbulent reattachment, the numerical data agree well with the experimental data, the size of the recirculation bubble and the peak heat flux are well predicted. From the slight offset observed and from a physical point of view, it is thought that the transition from laminar to turbulent actually occurs within the recirculation bubble.

T2-97 Hollow cylinder-flare

The flow pattern developing on the hollow cylinder-flare has strong similarities with the first test case, such as a shock wave boundary layer interaction and a large recirculation zone. The flow conditions are:

M_∞	9.91
Re_∞	$1.86 * 10^5/m$
T_∞	51 K
p_∞	6.3 Pa
T_{wall}	293 K
L	0.1017 m

which corresponds to a highly viscous flow and consequently relative thick boundary layers.

To illustrate the flow and the geometry, the pressure coefficient isolines are plotted in figure 11 where the computational domain has been mirrored around the symmetry axis. Note the complex flow pattern

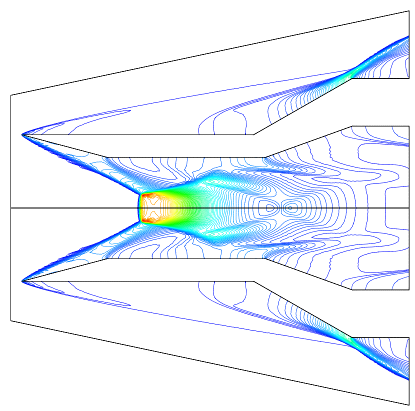

Fig. 11 Pressure coefficient isolines for T2-97

in the interior domain.

As the internal part of the flow has no influence on the external part, the finite volume code only computes the latter. Preliminar computations on this test case were performed indicating that the grids need to be highly clustered in the recirculation bubble vicinity. A very fine grid is used with 425*161 points, allowing 4 multigrid levels. The height of the first cell at the flare junction is $2.6 * 10^{-6}m$, which corresponds to a very fine discretisation.

For the residual distribution code, the entire flow is computed, mainly to see how the internal flow behaves.

As the residual distribution code is designed for unstructured grids, a hybrid structured/unstructured mesh is used.[19] Near the viscous walls a hyperbolic structured grid generator is used. As soon as the cells become isotropic, meshing is continued using a quadtree frontal Delaunay method. This mesh for this test case is made of 37356 nodes (73500 cells) with 586 faces on the solid wall boundary. The height of the first cell at the flare junction is $3 * 10^{-5}$m which is about 8 times larger than for the previously mentioned structured grid.

The convergence strategies used for the codes are similar to the ones used for the hyperboloid case: explicit time stepping with multigrid acceleration for the finite volume code, and implicit backward Euler for the residual distribution code, where the maximum CFL number has to be restricted to 10, because of the Mach stem in the interior flow field.

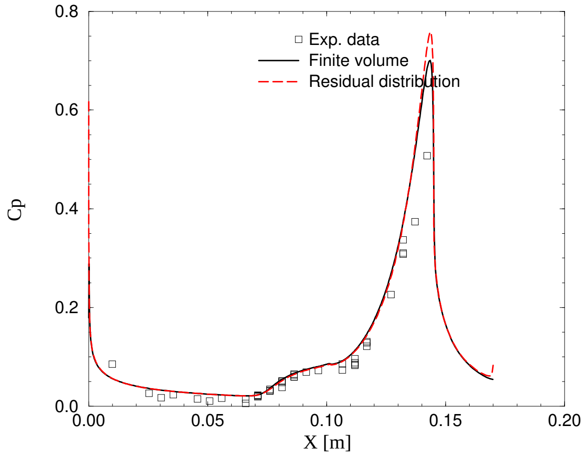

Fig. 12 Pressure coefficient on the hollow flare - Codes comparison for T1.97.1

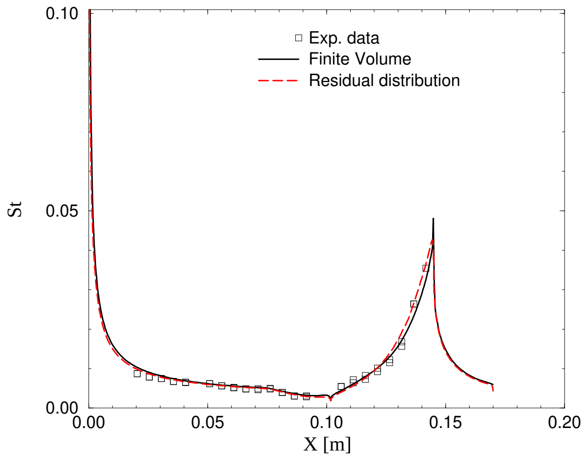

Fig. 13 Heat flux coefficient on the hollow flare - Codes comparison for T1.97.1

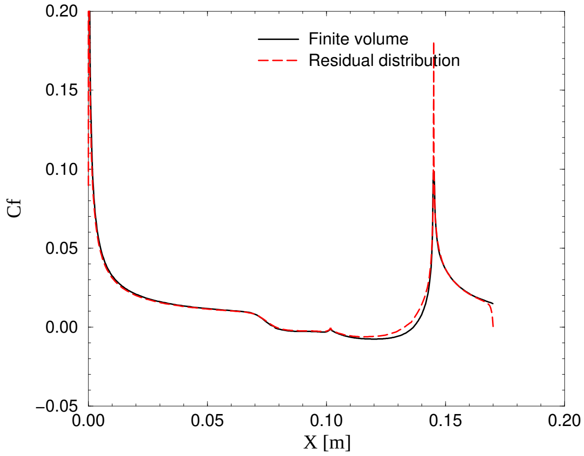

Fig. 14 Skin friction coefficient on the hollow flare - Codes comparison for T1.97.1

As seen in figures 12 and 13, the agreement of the two codes on different grids is very good. It can be noticed that the predicted size of the recirculation bubble is identical in the two cases. Also, this recirculation bubble is very large, as is expected because of the low Reynolds number. When compared to the experimental data,[20] the two flow solvers give a very good prediction for both the pressure and the heat flux coefficients.

The internal flow computed using the residual distribution code turns out to be of extreme complexity. First, we can notice a Mach stem which is known to be difficult to compute. Then the shocks are reflected onto the symmetry axis and bounce back towards the inner wall where a shock wave / boundary layer interaction is present and recirculation bubbles are formed.

The convergence history for the two codes is shown in figures 15 and 16.

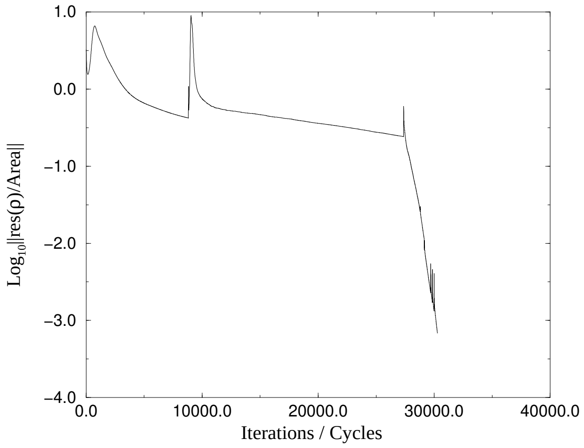

Fig. 15 Convergence history - Finite volume code

Again, the multigrid acceleration is seen to bring a very large improvement for the explicit time integration. It must be mentioned that, in the residual evaluation for the L_2 and the L_∞ norm in the finite volume code, the metrics are used. This emphasises the errors on the small grid cells.

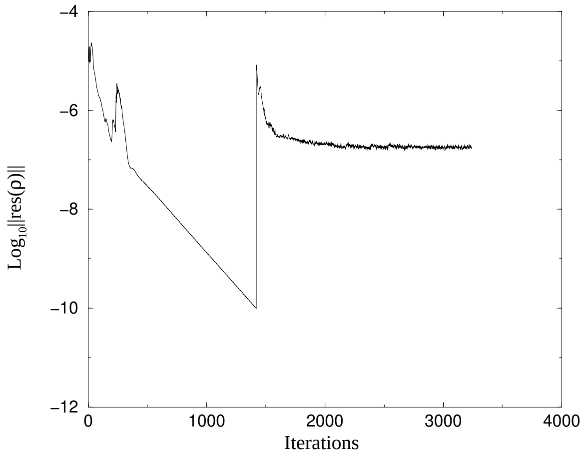

Fig. 16 Convergence history - Residual distribution code

$$L_2 = log_{10}\left(\sqrt{\sum(\frac{\rho}{Area})^2}\right) \tag{14}$$

In the standard definition, the metrics do not intervene, and it is the standard definition which is now implemented. The large number of implicit iterations of the residual distribution code is explained by the fact that the CFL number has to be limited to 10 to remain stable in the region of the Mach stem.

T3-97 Ogive Cylinder

This test case corresponds to a fully three dimensional flow. To simplify the problem, the base flow is not computed since it is known to give rise to many numerical problems. Two test cases are proposed, one for moderate angle of attack (10^o, test case T3-97.1) and the other one for a high angle of attack (20^o, test case T3-97.2). For both cases for which the wall surface is assumed to be adiabatic.

Moderate angle of attack

The flow conditions for this cases are:

M_∞	2.0
Re_∞	$5.33 * 10^6/m$
T^0_∞	330 K
p^0_∞	50000 Pa
α	10 deg
D	0.03 m

For the 3D finite volume solver (which is still under development), the grid is generated using first a 2 dimensional grid which is then extended through a rotation. The rotation is carried out with a variable radius and thus the grid is not circular. Because of the flow symmetry with respect to the longitudinal plane, only half of the domain needs to be constructed. To illustrate the grid properties, figure 17 shows a cut in the x,y plane for z=0. Then figure 18 shows a cut in the y,z plane for x=0.270 m. (i.e. the exit plane), the grid has been mirrored to emphasize the external boundary shape. The grid size is 101*51*31 (x,y,z) cells and it thus has 150000 nodes, the grid spacing at the wall varies along the body, as well as the stretching factor. At the ogive cylinder junction, the height of the first cell is about $2 * 10^{-5}$m.

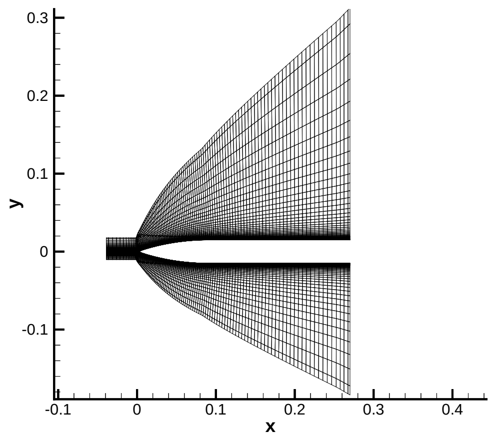

Fig. 17 Structured grid for the ogive cylinder, xy plane (z=0)

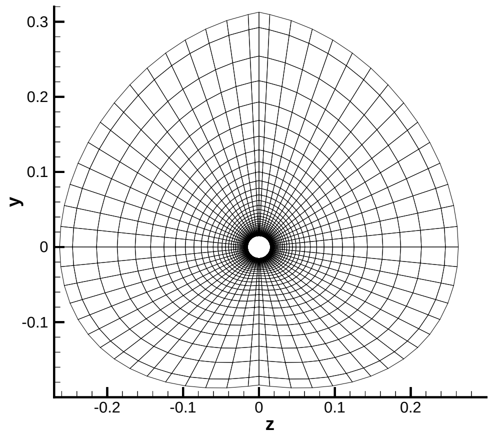

Fig. 18 Structured grid for the ogive cylinder, yz plane (x=0.270m)

The computation is first carried out solving the Euler equations to obtain a reasonable flow initialisation, using a forward Euler integration scheme (CFL=0.6). This is followed by a first order Navier-Stokes, and then by a second order Navier-Stokes computation for which a 4 step Runge-Kutta scheme is used (CFL=1.6).

The convergence history for this computation is shown in figure 19.

It is seen that the convergence gradually stalls out after two orders of magnitude showing the need for a multigrid acceleration. The vortices developing on the ogive cylinder and the associated separation are the probable cause for this. Figure 20 shows the Mach isolines contour and the velocity vectors in the

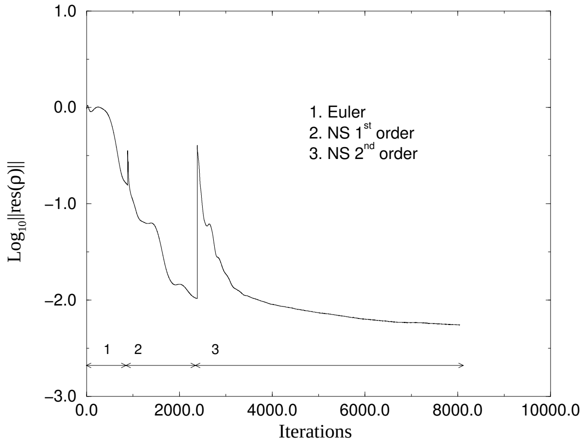

Fig. 19 Convergence history for the 3D FV solver - T3-97.1

exit plane illustrating the formation of the vortices and the separated region.

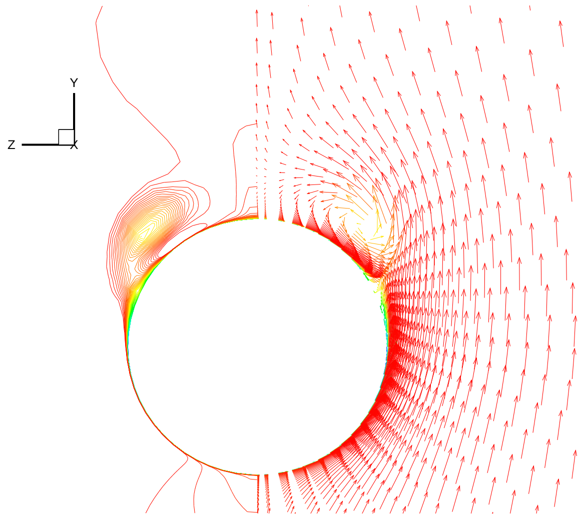

Fig. 20 Vortices and separation in the exit plane - 3D FV solver - T3-97.1

To illustrate the flow field over the ogive cylinder at 10 degrees angle of attack, Mach iso lines in various planes are shown in figure 21.

For the unstructured solver a fully unstructured grid has been generated using the FLITE3D grid generator of the University of Swansea.[21] Due to limitations of this grid generator a symmetry plane cannot be used and the full problem must be computed. The grid consist of 390,965 nodes (2,302,869 tetrahedra) from which 17,893 belong to the ogive cylinder surface grid, shown in figure 22. The initial normal spacing is $1.0*10^{-5}$ and the stretching factor is 1.2. To create a smooth transition from the viscous to the inviscid grid, 26 viscous layers have been used.

As the 3D parallel, implicit solver has not been fully tested yet, the computations have been done explicitly on 32 processors of the Cray T3E of the Technical University of Delft. The time integration method was forward Euler with a CFL number of 0.5. The convergence history is shown in figure 23.

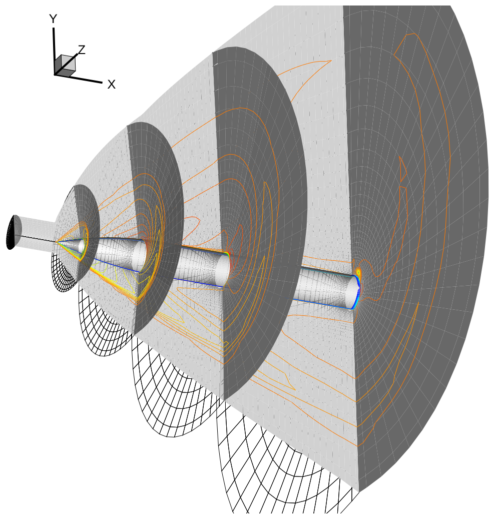

Fig. 21 Mach number isolines - 3D FV solver - T3-97.1

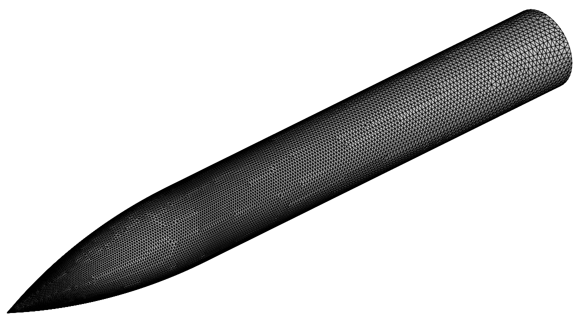

Fig. 22 Unstructured surface grid for the ogive-cylinder, 17,893 nodes

It can be seen from this figure that the first order

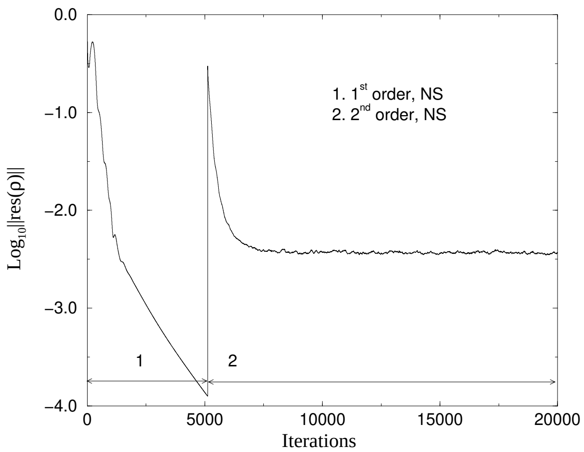

Fig. 23 Explicit convergence history for the T3-97.1 test case of the unstructured solver

solution is converging well, probably machine accuracy can be reached, but the nonlinear second order schemes stalls after 2 order of magnitude. The total CPU time for this problem is 27 hours. From experience in 2D for similar problems, laminar viscous flow and an attached shock, it is to be expected that this amount of time can be reduced by a factor of 10 for the implicit time integrator.

The two codes are compared for the wall pressure distribution in the longitudinal direction for three radial positions: $\theta = 0^o$ (on the top part), $\theta = 90^o$ (on the side) and $\theta = 180^o$ (on the lower part). In figure 24, it is seen that the two codes give wall pressures in a reasonable agreement. It is thought that the main cause for the differences is due to the grids employed (the unstructured mesh is 30% more dense than its structured counterpart).

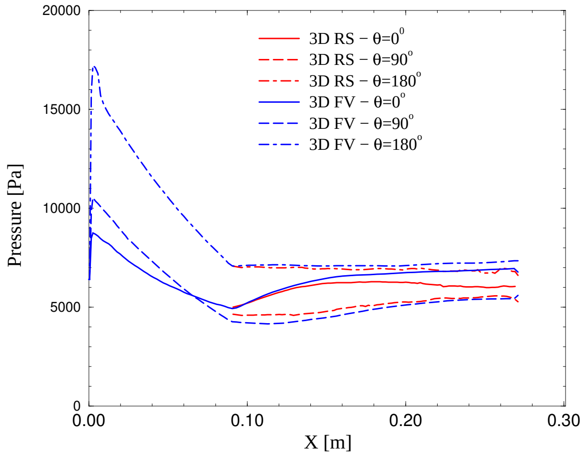

Fig. 24 Pressure distribution on the ogive-cylinder - 3D code comparison - T3-97.1

As expected, we see that the pressure decreases for decreasing θ.

High angle of attack

The angle of attack is increased from 10 degrees to 20 degrees. The flow conditions are similar to the first case. One expects to see larger vortices forming on the ogive cylinder upper surface. For this test case, only the 3 dimensional structured Navier-Stokes finite volume code is used.

For the 3D finite volume code, the grid is generated in a similar fashion except that the function to extend the 2 dimensional grid to 3 dimensions is larger. Thus the grid is more stretched on the leeward side and is closer to the wall on the windard part.

The flow over the ogive cylinder is very similar to the previous case except for the vortices which are larger. To emphasise the vortex, the streamtraces are plotted instead of the velocity vectors. This is shown in figure 25 for the exit plane (see figure 20 for comparison).

For the wall pressure, it is expected to see a sharp drop of pressure on the upper part whereas the pressure on the lower part of the body should be higher (see figure 26).

From this figure, it is also seen that on the sides of the ogive cylinder (i.e. for θ=90^o), the wall pressure

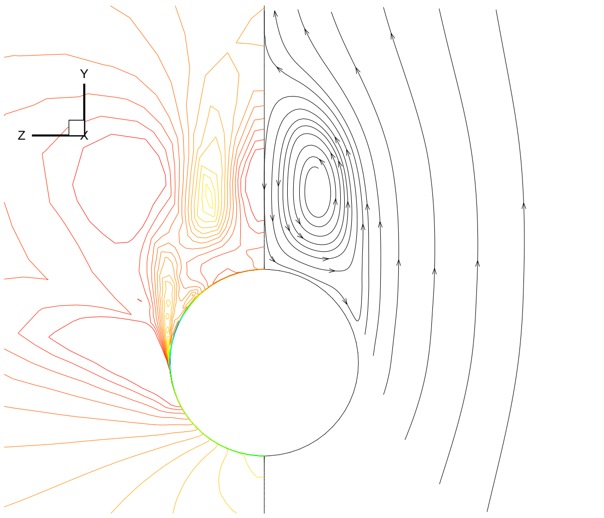

Fig. 25 Vortices and separation in the exit plane - 3D FV solver - T3-97.2

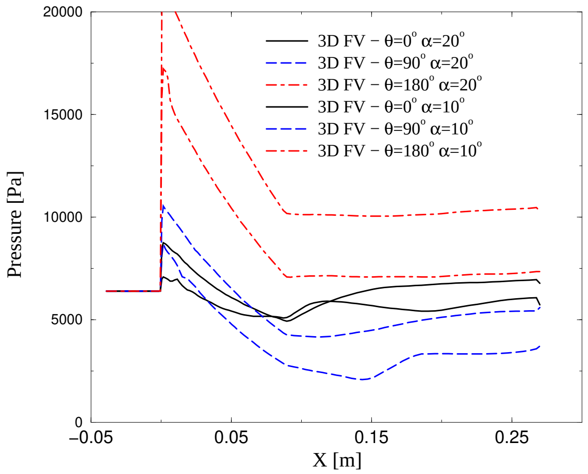

Fig. 26 Pressure distribution on the ogive-cylinder - T3-97.1 vs. T3-97.2 - 3D FV code

for the 20^o angle of attack case is still substantially lower than for the 10^o case.

Conclusion

A structured grid finite volume code and an unstructured grid residual distribution code, both developed at the VKI have been presented and compared for a wide range of flow conditions including supersonic / hypersonic as well as laminar / turbulent flow regimes.

For the axisymmetric cases, the modeling of the recirculation bubble and the assiocated flow field has shown that the codes are able to provide very accurate predictions (e.g hollow flare cylinder case).

For the hypersonic turbulent regime of the hyperboloid-flare, a good prediction can be achieved (e.g peak heat flux) but some more work has to be done especially for the modeling of turbulence.

The comparisons of the two axisymmetric codes has shown that the residual distribution code based on unstructured grids can achieve the same level of accuracy as standard finite volume codes based on qualidratelals.

Convergence acceleration techniques such as the multigrid or the backward Euler fully implicit time integrator have shown to bring large reductions in the computational time.

Three dimensional test cases have been computed for laminar and turbulent supersonic flow regimes. Much experience has been gained when computing these cases. First, grid generation is one of the most important key elements in 3D and unstructured grids are very attractive. The very fine spatial discretizations of 2D/axisymmetric cases can not be employed in 3D for computational time reasons and thus relatively coarse grids must be employed. The number of points necessary in 3D makes the use of acceleration techniques mandatory and one can not use simple standard explicit schemes for large problems. Implicit methods have shown to be very attractive but they require a tremendous amount of data storage and therefore parallel implicit solvers are better suited for complex 3D cases.

References

[1] C. Mensink. A 2-D Parallel MultiBlock Method for Viscous and Inviscid Compressible Flow. *PhD Thesis VKI/U. Twente, December 1992.*

[2] F. Coquel; M. Liou. Field by Field Hybrid Upwind Splitting Methods. *AIAA, Vol. 93-3302-CP, 1993.*

[3] P.R. Spalart; S.R. Allmaras. A one-equation turbulence model for aerodynamic flows. *La Recherche Aerospatiale, 1994 n° 1, 5-21.*

[4] R. Paciorri; W. Dieudonné; G. Degrez; J.-M. Charbonnier and H. Deconinck. Exploring the validity of the Spalart-Allmaras turbulence model for hypersonic flows. *AIAA Journal, to be published.*

[5] W. Dieudonné; J.M. Charbonnier; H.Deconinck. ESA/MSTP Workshop 96: Test Case III.b: Hyperboloid-Flare Standard Model at RWG Reference Calibration Point. *ESA/MSTP Workshop 1996 on Reentry Aerothermodynamics and Ground-to-Flight Extrapolation, March 1996.*

[6] D.J. Mavriplis. Multigrid techniques for unstructured meshes. *Computational Fluid Dynamics. VKI Lecture Series 1995-02.*

[7] D.J. Mavriplis; V. Venkatakrishnan. A 3D Agglomeration multigrid solver for the Reynolds-Averaged Navier-Stokes equations on unstructured meshes. *International Journal for Numerical Methods in Fluids, Vol. 23, 527-544 (1996).*

[8] W. Dieudonné. Implementation of an explicit multidomain multigrid scheme for the VKI-MB code. *June 1997, VKI Technical Report, to be published.*

[9] H. Deconinck, R. Struijs, G. Bourgois, and P.L. Roe. Compact advection schemes on unstructured grids. In *VKI LS 1993-04, Computational Fluid Dynamics*, 1993.

[10] H. Paillère and H. Deconinck. Compact multidimensional upwind convection schemes on unstructured meshes. *Conf. on Num. Meth. for Euler and N-S equations, Montreal, Canada*, 1995.

[11] H. Paillère, H. Deconinck, and E. van der Weide. Upwind Residual Distribution methods for compressible flow: An alternative to Finite Volume and Finite Element methods. *Part I: scalar schemes* . In *VKI LS 1997-02, Computational Fluid Dynamics*, 1997.

[12] E. van der Weide and H. Deconinck. Positive Matrix Distribution Schemes for Hyperbolic Systems, with application to the Euler Equations. pages 747–753. Wiley, 1996. Proceedings of the 3rd European CFD Conference.

[13] E. van der Weide and H. Deconinck. Upwind Residual Distribution methods for compressible flow: An alternative to Finite Volume and Finite Element methods. *Part II: System Schemes and Applications* . In *VKI LS 1997-02, Computational Fluid Dynamics*, 1997.

[14] J.-C. Carette, H. Deconinck, H. Paillère, and P. L. Roe. Multidimensional upwinding : Its relation to finite elements. *Int. J. of Num. Meth. Fluids*, 20:935–955, 1995.

[15] S. Hutchinson; J. Shadid; R. Tuminaro. Aztec User's Guide. *Massively Parallel Computing Research Laboratory, Sandia National Laboratories Albuquerque - SAND 95-1559.*

[16] F. R. Menter. Two-Equation Eddy-Viscosity Turbulence Models for Engineering Applications. *AIAA journal, Vol. 32, No. 8, August 1994.*

[17] P. Krogmann. Calibration and Validation Measurements in the Ludwieg Tube Tunnel B (RWG). *ESA/CNES HT-TR-E-1-301-DGLR, DLR, July 1996.*

[18] P. Krogmann. Hyperboloid-Flare experiments at Mach 6.8 in RWG. *Technical Note HT-TN-0-2074-DLR, September 1994.*

[19] J. C. Carette. Adaptive unstructured mesh algorithms and SUPG finite element method for high Reynolds number compressible flows. *PhD Thesis VKI/ULB, December 1997.*

[20] B. Chanetz. Study of axisymmetric shock wave/boundary layer interaction in hypersonic laminar flow. *ONERA Technical report RT 42/4362 AN, February 1995.*

[21] O. Hassan; K. Morgan; E.J. Probert; J. Peraire. Unstructured tetrahedral mesh generation for three-dimensional viscous flows. *International jorunal for numerical methods in engineering, vol. 39, 549-567 (1996).*